Available online at www.sciencedirect.com
SCIENCE DIRECT®
International Journal of Heat and Mass Transfer 48 (2005) 5431–5445
International Journal of HEAT and MASS TRANSFER
www.elsevier.com/locate/ijhmt

Thermodynamic analysis of near-wall effects on phase stability and homogeneous nucleation during rapid surface heating

V.P. Carey [a,*], A.P. Wemhoff [b]

[a] Mechanical Engineering Department, University of California, Berkeley, CA, United States
[b] New Technologies Engineering Division, Lawrence Livermore National Laboratory, Livermore, CA, United States

Received 28 October 2004; received in revised form 24 June 2005
Available online 29 August 2005

Abstract

Rapid heating of a liquid by a thin film heater surface may initiate homogeneous nucleation of vapor in the liquid in contact with the surface. In such circumstances, nucleation is generally expected to be most likely in the hottest liquid closest to the surface. It is known, however, that in many cases the liquid molecules closest to the surface will experience long-range attractive forces to molecules in the solid, with the result that the equation of state for the liquid near the surface will differ from that for the bulk liquid. In the investigation summarized here, a statistical thermodynamics analysis was used to derive a modified version of the Redlich–Kwong fluid property model that accounts for attractive forces between the solid surface molecules and liquid molecules in the near-wall region. In this model, the wall–fluid attractive forces are quantified in terms of Hamaker constants. This feature makes it possible to assess the effect of wall–fluid force interactions on the spinodal conditions for a variety of fluid and surface material combinations. The variation of pressure near the wall predicted by this model agrees well with the predictions of a hydrostatic model and molecular dynamics simulations. The results of the thermodynamic model analysis indicate that force interactions are important for a wide variety of fluids only within a few nanometers of the solid surface. The model specifically predicts that these forces increase the spinodal temperature in the near-surface region. The implications of this increase for nucleation near a solid surface during rapid heating are explored for circumstances similar to those in inkjet printer heads. The results of the analysis imply that during rapid transient heating, wall effects can result in homogeneous nucleation occurring first at a location slightly away from the solid surface. The results further suggest that on rough surfaces, wall effects may play a role in making some cavities preferred sites for homogeneous nucleation.
© 2005 Elsevier Ltd. All rights reserved.

Keywords: Homogeneous nucleation; Wall effects; Rapid heating; Redlich–Kwong; Thermodynamic spinodal; Molecular dynamics

1. Introduction

Transient boiling is important in many situations of technological interest, including the transient initiation of a steady boiling process in evaporators and the rapid heating to produce nucleation and bubble growth in inkjet printer droplet generators and MEMS bubble pumps. Heating the wall above the saturation temperature may give rise to heterogeneous nucleation or homogeneous nucleation of bubbles at the interface between the liquid and the solid wall. In circumstances where homogeneous nucleation is expected (highly-wetting liquids and/or

* Corresponding author.
E-mail address: vcarey@me.berkeley.edu (V.P. Carey).

0017-9310/$ - see front matter © 2005 Elsevier Ltd. All rights reserved.
doi:10.1016/j.ijheatmasstransfer.2005.06.027

Nomenclature

a_R, b_R	Redlich–Kwong coefficients
A_{ll}	liquid–liquid Hamaker constant
A_{ls}	liquid–solid Hamaker constant
$C_{\phi,ff}$	fluid–fluid attractive force potential coefficient
$C_{\phi,fs}$	fluid–solid attractive force potential coefficient
D_f	fluid molecule effective diameter
D_m	mean effective molecular diameter
D_s	solid molecule effective diameter
h	Planck's constant
J	rate of formation of embryos of critical size
k_l	liquid thermal conductivity
k_s	solid thermal conductivity
k_B	Boltzmann's constant
M	molecular mass
N	number of molecules
N_A	Avogadro's number
P	pressure
P_c	critical pressure
q''	heat flux
Q	canonical partition function
R	universal gas constant, $N_A k_B$
t	time
T	temperature
T_c	critical temperature
T_{spin}	spinodal temperature
$\hat{v}$	molar specific volume
$\hat{v}_c$	critical molar specific volume
V	volume
r_{ij}	distance between molecules i and j in the radial direction
Z_N	classical configuration integral
α_l	liquid thermal diffusivity
α_s	solid thermal diffusivity
ϕ_{ff}	fluid–fluid intermolecular potential
ϕ_{LJ}	Lennard-Jones 6–12 intermolecular potential
ϕ_{sf}	solid–fluid intermolecular potential
$\theta_{rot,m}$	mean rotational temperature
$\hat{\rho}$	molar density
$\hat{\rho}_c$	critical molar density
σ_{lv}	interfacial tension
σ_{LJ}, ε_{LJ}	Lennard-Jones 6–12 potential length and energy parameters
σ_s	symmetry number
ξ	number of translational and rotational storage modes
$\hat{\mu}$	molar chemical potential

extremely smooth surfaces), conventional homogeneous nucleation theory suggests that homogeneous nucleation is most likely to occur at the solid surface where the liquid is most highly superheated.

Skripov [1] and Asai [2] observed that under extremely high heat flux pulse heating, the dominant bubble generation mechanism is the spontaneous nucleation due to thermal motion of liquid molecules (homogeneous nucleation). Andrews and O'Horo [3,4] experimentally found that rapid transient heating of a film heater in contact with liquid produced some bubbles by heterogeneous nucleation and some bubbles by homogeneous nucleation. Lin et al. [5] also concluded that sudden energizing of polysilicon microresistors in fluorinert liquids also resulted in formation of a bubble by homogeneous nucleation.

A particularly interesting result of the investigation by Andrews and O'Horo [3] is that they reported observing bubble formation by homogeneous nucleation on or near the heater surface during the heating transient. The occurrence of homogeneous nucleation away from the surface would seem to contradict the expectation that homogeneous nucleation, if it occurs, will take place first at the surface itself where the liquid is superheated the most. For this observation to be correct, there would have to be a mechanism that suppresses homogeneous nucleation very near the wall, or makes it more likely some distance away from it. One possibility is that force interactions between molecules of the liquid and molecules in the solid surface are affecting the state of the fluid in a way that modifies the intrinsic stability limit.

The effects of long-range force interactions between molecules in a fluid phase and the molecules in a nearby solid wall have been widely studied [6]. Specifically, the long-range attractive dispersion force interactions are known to attract fluid molecules to the solid surface. These attractive forces facilitate the formation of adsorbed liquid films on solid surfaces and disjoining pressure effects in ultra-thin liquid films [6]. Gerweck and Yadigaroglu [7] developed an analytical model of the effects of these attractive forces on the equation of state of the fluid. They used a thermodynamic analysis to assemble an equation of state by combining a repulsive force interaction model for a hard sphere fluid with attractive force models for interactions between the fluid molecules and solid surface molecules. Their analysis is cast in terms of an inverse characteristic length, which is unspecified. Gerweck and Yadigaroglu [7] argued that this characteristic length can be determined from contact angle and liquid surface tension data. They concluded that the length scale is of the order of a molecular diameter, but no specific values were provided.

Although it is difficult to extract specific predictions from the study of Gerweck and Yadigaroglu [7], it does provide qualitative predictions of the effect of attractive forces near the wall. It predicts that for typical conditions, the pressure is very high near the wall. With increasing distance from the wall, their model predicts that the pressure drops and becomes negative and then rises to the bulk liquid value in the far field. This model analysis thus predicts that a supercritical region exits very close to the wall and a region in which the fluid is in tension exists between this supercritical region and the bulk fluid. As the wall is approached, the local spinodal temperature is predicted to first decrease and then increase very near the wall. The authors argue that the minimum in the spinodal temperature is associated with the first appearance of vapor via homogeneous nucleation in a rewetting process.

While the model of Gerweck and Yadigaroglu [7] provides some interesting insight into the effects of attractive forces in the near-wall region, the model incorporates several idealizations that have not been extensively tested, and its predictions of a supercritical region and tension region of negative pressure near the surface have not been compared to predictions of other models. The investigation summarized here sought to verify the predictions of this analysis by an alternate approach.

2. Thermodynamic analysis

The objective of the investigation summarized here was to construct a model equation of state for the liquid that accounts for long-range attraction forces between molecules in the fluid and molecules in a nearby solid wall. In this investigation, a form of the Redlich–Kwong fluid property model was developed in which the attractive force interaction effects were included for the near-wall region. The Redlich–Kwong fluid property model was selected because it is generally acknowledged to be a better predictor for properties near saturation conditions than the well-known van der Waals model. In addition, the spinodal curve predicted by the Redlich–Kwong model agrees fairly well with the onset of homogeneous nucleation conditions for a number of fluids (see, for example, the data in Fig. 1).

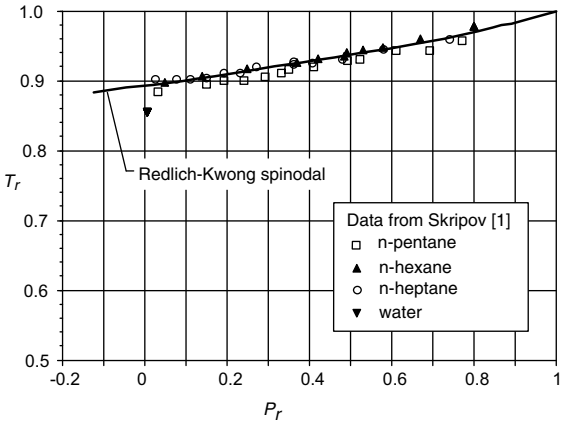

Fig. 1. Comparison of the Redlich–Kwong fluid model spinodal curve to experimental homogeneous nucleation data.

Carey [8] has shown that for the Redlich–Kwong fluid model, standard statistical thermodynamic analysis can be used to derive the following relation for the natural log of the canonical partition function.

$$\ln Q = N + \left(\frac{3N}{2}\right)\ln\left[\frac{2\pi M k_B T}{N^{2/3}h^2}\right] + N\left[\frac{\xi-5}{2}\ln\pi - \ln\sigma_s\right] + \frac{(\xi-3)N}{2}\ln\left(\frac{T}{\theta_{rot,m}}\right) + \ln Z_N \quad (1)$$

In the above equation, h is Planck's constant, k_B is the Boltzmann constant, M is the molecular mass of the molecule, ξ is the number of translational and rotational storage modes, σ_s is the symmetry number for the molecule, $\theta_{rot,m}$ is the mean rotational temperature for the molecule if it is a polyatomic species [8], and Z_N is the classical configuration integral. Carey [8] further showed that the configuration integral is given by

$$Z_N = e^{-\Phi_{N,RK}/k_B T}(V - Nb_R)^N \quad (2)$$

where $\Phi_{N,RK}$ is the total potential energy due to attractive and repulsive force interactions among the N molecules in the system volume and their neighbors for the Redlich–Kwong fluid.

We consider now a system of fluid molecules with volume V at a distance z from a plane surface s^*, as indicated in Fig. 2a. In this circumstance, the potential energy in the system is only due to interactions with surrounding fluid molecules. For liquid near a solid surface, as in Fig. 2b, we assume that interactions between the solid and fluid molecules obey the Lennard-Jones type potential function

$$\phi_{fs}(r) = -\frac{C_{\phi,fs}}{r^6}\left[1 - \gamma\frac{D_m^6}{r^6}\right] \quad (3)$$

This potential function incorporates an attractive force potential that is proportional to r^{-6} and a close range repulsive force component that decays proportional to r^{-12}. The Lennard-Jones potential was selected because it is generally acknowledged to be among the more realistic two-parameter potential function models. Because it is a two-parameter model, use of the Lennard-Jones potential is consistent with the two-parameter Redlich–Kwong property model used here. In Eq. (3), $C_{\phi,fs}$ is the attractive force potential coefficient and D_m is the mean effective diameter defined as

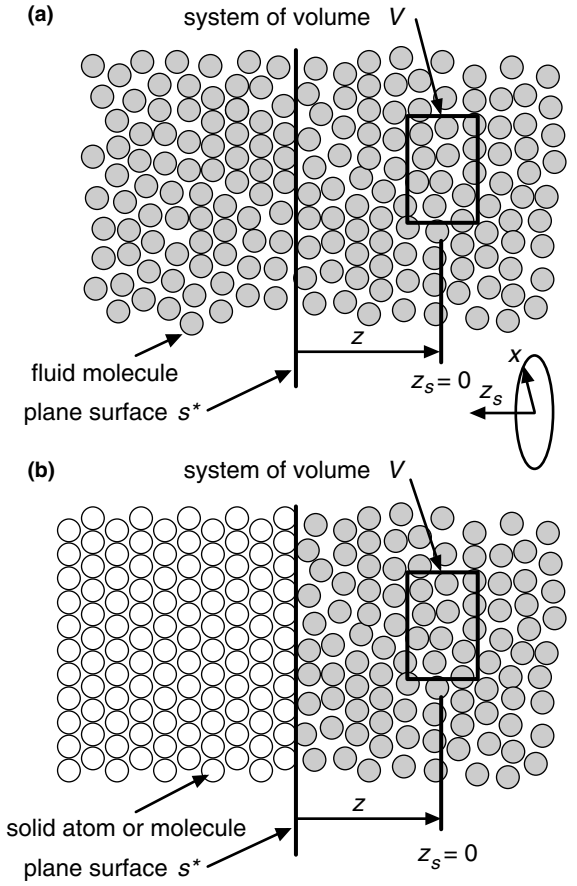

Fig. 2. Schematics for analysis of intermolecular interactions in the near-wall region.

$$D_{\mathrm{m}} = \frac{D_{\mathrm{s}} + D_{\mathrm{f}}}{2} \tag{4}$$

where D_{s} and D_{f} are the effective diameters of the solid and liquid phase molecules, respectively. The constant γ in Eq. (3) modifies the repulsive component, adjusting the r position of the minimum in the potential well. Here γ is taken to be one, so the minimum of the potential well is at $r = r_{\min} = 2^{1/6} D_{\mathrm{m}}$, consistent with a typical Lennard-Jones 6–12 potential.

$$\phi_{\mathrm{fs}}(r) = -\frac{C_{\phi,\mathrm{fs}}}{r^6}\left[1 - \frac{D_{\mathrm{m}}^6}{r^6}\right] \tag{5}$$

We further assume that a similar form, with different constants, models the force interaction between a pair of two fluid molecules.

$$\phi_{\mathrm{ff}}(r) = -\frac{C_{\phi,\mathrm{ff}}}{r^6}\left[1 - \frac{D_{\mathrm{f}}^6}{r^6}\right] \tag{6}$$

In the liquid and solid phases of interest here, the interactions between pairs of molecules are treated as independent and additive.

We next consider the change in system potential energy (work) required to move the fluid molecules to the left of the plane s^* in Fig. 2a to an infinite separation against the (negative) attractive force of one fluid molecule at a distance z from the plane. To get this change in system potential, we spatially integrate the product of the density and the negative of the molecular potential to sum the contributions of each fluid molecule on the left side.

$$\Delta\Phi_{\mathrm{fmf}} = \int_{z_s=z}^{z_s=\infty}\int_{x=0}^{x=\infty} \rho_{N,\mathrm{f}} \frac{C_{\phi,\mathrm{ff}}}{\left(x^2+z_{\mathrm{s}}^2\right)^3}(2\pi x)\,\mathrm{d}x\,\mathrm{d}z_{\mathrm{s}} - \int_{z_s=z}^{z_s=\infty}\int_{x=0}^{x=\infty} \rho_{N,\mathrm{f}} \frac{C_{\phi,\mathrm{ff}} D_{\mathrm{f}}^6}{\left(x^2+z_{\mathrm{s}}^2\right)^6}(2\pi x)\,\mathrm{d}x\,\mathrm{d}z_{\mathrm{s}} \tag{7}$$

Here $\rho_{N,\mathrm{f}} = N/V$ is the number density of molecules in the fluid. The additional subscript f denotes the density for the fluid. Executing the integrals with $\rho_{N,\mathrm{f}}$ and $C_{\phi,\mathrm{ff}}$ taken to be constants, the relation for the change in system potential becomes

$$\Delta\Phi_{\mathrm{fmf}} = \frac{\pi\rho_{N,\mathrm{f}} C_{\phi,\mathrm{ff}}}{6z^3} - \frac{\pi\rho_{N,\mathrm{f}} C_{\phi,\mathrm{ff}} D_{\mathrm{f}}^6}{45z^9} \tag{8}$$

For the molecules in volume V at a distance z from the surface, the total potential change (work) required to remove the molecules to the left of plane s^* is the work per fluid molecule multiplied by the number of molecules in the volume, $\rho_{N,\mathrm{f}} V$. With a bit of rearranging, the resulting equation is

$$\Delta\Phi_{\mathrm{fVf}} = \frac{\pi\rho_{N,\mathrm{f}}^2 C_{\phi,\mathrm{ff}} V}{6z^3}\left[1 - \frac{2D_{\mathrm{f}}^6}{15z^6}\right] \tag{9}$$

The same line of reasoning leads to the conclusion that the potential energy change of the system as an array of solid molecules or atoms is brought to the surface s^* of the liquid is given by

$$\Delta\Phi_{\mathrm{fVss}} = -\frac{\pi\rho_{N,\mathrm{s}}\rho_{N,\mathrm{f}} C_{\phi,\mathrm{fs}} V}{6z^3}\left[1 - \frac{2D_{\mathrm{m}}^6}{15z^6}\right] \tag{10}$$

where $\rho_{N,\mathrm{s}}$ is the bulk solid number density. The negative sign in Eq. (10) arises because the system does work as the solid molecules are moved into place, reducing the system energy. Summing the changes $\Delta\Phi_{\mathrm{fVss}}$ and $\Delta\Phi_{\mathrm{fVf}}$ yields the net change in the potential function for the fluid volume due to replacing the liquid to the left of the plane by the solid.

$$\Delta\Phi_V = \frac{\pi\rho_{N,\mathrm{f}}^2 C_{\phi,\mathrm{ff}} V}{6z^3}\left[1 - \frac{2D_{\mathrm{f}}^6}{15z^6}\right] - \frac{\pi\rho_{N,\mathrm{s}}\rho_{N,\mathrm{f}} C_{\phi,\mathrm{fs}} V}{6z^3}\left[1 - \frac{2D_{\mathrm{m}}^6}{15z^6}\right] \tag{11}$$

For convenience, we reorganize this relation in terms of modified Hamaker constants defined as

$$\tilde{A}_{\mathrm{ll}} = \pi^2\rho_{N,\mathrm{fc}}^2 C_{\phi,\mathrm{ff}}, \quad \tilde{A}_{\mathrm{ls}} = \pi^2\rho_{N,\mathrm{fc}}\rho_{N,\mathrm{s}} C_{\phi,\mathrm{fs}} \tag{12}$$

where $\rho_{N,\mathrm{fc}}$ is the fluid density at its critical point. It should be noted that the conventional Hamaker constants associated with liquid–liquid and liquid–solid molecular interactions, A_{ll} and A_{ls}, respectively, are defined as

$$A_{\mathrm{ll}} = \pi^2 \rho_{N,\mathrm{f}}^2 C_{\phi,\mathrm{ff}}, \quad A_{\mathrm{ls}} = \pi^2 \rho_{N,\mathrm{f}} \rho_{N,\mathrm{s}} C_{\phi,\mathrm{fs}} \tag{13}$$

Comparing the above relations to Eq. (12), it is clear that $\tilde{A}_{\mathrm{ll}} = A_{\mathrm{ll}} \rho_{N,\mathrm{fc}}^2 / \rho_{N,\mathrm{f}}^2$ and $\tilde{A}_{\mathrm{ls}} = A_{\mathrm{ls}} \rho_{N,\mathrm{fc}} / \rho_{N,\mathrm{f}}$, which make it possible to convert the modified Hamaker constants based on critical density to conventional Hamaker constants for the system. Using the definitions of $\tilde{A}_{\mathrm{ll}}$ and $\tilde{A}_{\mathrm{ls}}$, Eq. (11) then becomes

$$\Delta\Phi_V = \frac{\tilde{A}_{\mathrm{ll}} \rho_{N,\mathrm{f}}^2 V}{6\pi z^3 \rho_{N,\mathrm{fc}}^2} \left[1 - \frac{2D_{\mathrm{f}}^6}{15z^6}\right] - \frac{\tilde{A}_{\mathrm{ls}} \rho_{N,\mathrm{f}} V}{6\pi z^3 \rho_{N,\mathrm{fc}}} \left[1 - \frac{2D_{\mathrm{m}}^6}{15z^6}\right] \tag{14}$$

For the fluid in the near-wall region, the total potential is the bulk fluid potential $\Phi_{N,\mathrm{RK}}$ plus the wall effect correction $\Delta\Phi_V$ above. The configuration integral Z_N is therefore given by

$$Z_N = \exp\{-(\Phi_{N,\mathrm{RK}} + \Delta\Phi_V)/k_{\mathrm{B}}T\}(V - Nb_{\mathrm{R}})^N \tag{15}$$

For a bulk Redlich–Kwong fluid, the potential function $\Phi_{N,\mathrm{RK}}$ is given by [8]

$$\Phi_{N,\mathrm{RK}} = -\frac{a_{\mathrm{R}} N}{b_{\mathrm{R}} T^{1/2}} \ln\left(\frac{V + Nb_{\mathrm{R}}}{V}\right) \tag{16}$$

Combining Eqs. (14)–(16), we obtain

$$Z_N = \exp\left\{\frac{a_{\mathrm{R}} N}{b_{\mathrm{R}} T^{1/2} k_{\mathrm{B}} T} \ln\left(\frac{V + Nb_{\mathrm{R}}}{V}\right) - \frac{\tilde{A}_{\mathrm{ll}} \rho_{N,\mathrm{f}}^2 V}{6\pi z^3 \rho_{N,\mathrm{fc}}^2 k_{\mathrm{B}} T} \times \left[1 - \frac{2D_{\mathrm{f}}^6}{15z^6}\right] + \frac{\tilde{A}_{\mathrm{ls}} \rho_{N,\mathrm{f}} V}{6\pi z^3 \rho_{N,\mathrm{fc}} k_{\mathrm{B}} T} \left[1 - \frac{2D_{\mathrm{m}}^6}{15z^6}\right]\right\} \times (V - Nb_{\mathrm{R}})^N \tag{17}$$

Substituting the right side of Eq. (17) into Eq. (1), and using the fact that $\rho_{N,\mathrm{f}} = N/V$, the relation for the partition function becomes

$$\ln Q = N + \left(\frac{3N}{2}\right) \ln\left[\frac{2\pi M k_{\mathrm{B}} T}{N^{2/3} h^2}\right] + N\left[\frac{\xi - 5}{2} \ln\pi - \ln\sigma_{\mathrm{s}}\right] + \frac{(\xi - 3)N}{2} \ln\left(\frac{T}{\theta_{\mathrm{rot,m}}}\right) + \frac{a_{\mathrm{R}} N}{b_{\mathrm{R}} T^{1/2} k_{\mathrm{B}} T} \ln\left(\frac{V + Nb_{\mathrm{R}}}{V}\right) + N \ln(V - Nb_{\mathrm{R}}) - \frac{\tilde{A}_{\mathrm{ll}} N^2}{6\pi z^3 \rho_{N,\mathrm{fc}}^2 V k_{\mathrm{B}} T}\left[1 - \frac{2D_{\mathrm{f}}^6}{15z^6}\right] + \frac{\tilde{A}_{\mathrm{ls}} N}{6\pi z^3 \rho_{N,\mathrm{fc}} k_{\mathrm{B}} T}\left[1 - \frac{2D_{\mathrm{m}}^6}{15z^6}\right] \tag{18}$$

The equation of state and the relation for the chemical potential are obtained from Eq. (18) using the following standard property relations from statistical thermodynamics [8]

$$P = k_{\mathrm{B}} T \left(\frac{\partial \ln Q}{\partial V}\right)_{T,N} \tag{19}$$

$$\hat{\mu} = -N_{\mathrm{A}} k_{\mathrm{B}} T \left(\frac{\partial \ln Q}{\partial N}\right)_{T,V} \tag{20}$$

Taking the V and N derivatives of Eq. (18) and substituting them into Eqs. (19) and (20), respectively, and using the definitions of the molar density $\hat{\rho} = \rho/N_{\mathrm{A}} = (N/N_{\mathrm{A}})/V$, the following equations of state are obtained:

$$P = \frac{\hat{\rho} RT}{1 - \hat{\rho} b_{\mathrm{R}} N_{\mathrm{A}}} - \frac{\hat{\rho}^2 a_{\mathrm{R}} N_{\mathrm{A}}^2}{T^{1/2}(1 + \hat{\rho} b_{\mathrm{R}} N_{\mathrm{A}})} + \frac{\tilde{A}_{\mathrm{ll}} N_{\mathrm{A}}^2 \hat{\rho}^2}{6\pi z^3 \rho_{N,\mathrm{fc}}^2}\left[1 - \frac{2D_{\mathrm{f}}^6}{15z^6}\right] \tag{21}$$

$$\hat{\mu} = -RT\left[\frac{\xi - 5}{2} \ln\pi - \ln\sigma_{\mathrm{s}}\right] - RT \ln\left[\frac{1 - \hat{\rho} N_{\mathrm{A}} b_{\mathrm{R}}}{\hat{\rho} N_{\mathrm{A}} \Lambda^3}\right] + \frac{\hat{\rho} N_{\mathrm{A}} b_{\mathrm{R}} RT}{1 - \hat{\rho} N_{\mathrm{A}} b_{\mathrm{R}}} - \frac{(\xi - 3)RT}{2} \ln\left(\frac{T}{\theta_{\mathrm{rot,m}}}\right) - \frac{a_{\mathrm{R}} N_{\mathrm{A}}^2}{N_{\mathrm{A}} b_{\mathrm{R}} T^{1/2}} \ln(1 + \hat{\rho} N_{\mathrm{A}} b_{\mathrm{R}}) - \frac{a_{\mathrm{R}} N_{\mathrm{A}}^2}{T^{1/2}}\left(\frac{\hat{\rho}}{1 + \hat{\rho} N_{\mathrm{A}} b_{\mathrm{R}}}\right) + \frac{\tilde{A}_{\mathrm{ll}} N_{\mathrm{A}}^2 \hat{\rho}}{3\pi z^3 \rho_{N,\mathrm{fc}}^2}\left[1 - \frac{2D_{\mathrm{f}}^6}{15z^6}\right] - \frac{\tilde{A}_{\mathrm{ls}} N_{\mathrm{A}}}{6\pi z^3 \rho_{N,\mathrm{fc}}}\left[1 - \frac{2D_{\mathrm{m}}^6}{15z^6}\right] \tag{22}$$

where

$$\Lambda = \left[\frac{h^2}{2\pi M k_{\mathrm{B}} T}\right]^{1/2} \tag{23}$$

The Redlich–Kwong equation of state (21) in the bulk fluid away from the wall (large z) is

$$P = \frac{\hat{\rho} RT}{1 - \hat{\rho} b_{\mathrm{R}} N_{\mathrm{A}}} - \frac{\hat{\rho}^2 a_{\mathrm{R}} N_{\mathrm{A}}^2}{T^{1/2}(1 + \hat{\rho} b_{\mathrm{R}} N_{\mathrm{A}})} \tag{24}$$

For a Redlich–Kwong fluid, it is readily shown that

$$\hat{\rho}_{\mathrm{c}} RT_{\mathrm{c}}/P_{\mathrm{c}} = 3 \tag{25}$$

Using this relation with the equation of state, and invoking the zero slope and inflection point conditions for isotherms on a P–$\hat{v}$ plot passing through the critical point, it can be shown that a_{R} and b_{R} are related to the critical temperature and pressure as

$$a_{\mathrm{R}} = 0.42748 \frac{k_{\mathrm{B}}^2 T_{\mathrm{c}}^{2.5}}{P_{\mathrm{c}}}, \quad b_{\mathrm{R}} = 0.08664 \frac{k_{\mathrm{B}} T_{\mathrm{c}}}{P_{\mathrm{c}}} \tag{26}$$

The spinodal condition at the limit of intrinsic stability can be written in the form [8]

$$\left(\frac{\partial P}{\partial \hat{\rho}}\right)_T = 0 \tag{27}$$

Using Eq. (21), the spinodal condition requirement (27) becomes

$$\frac{RT}{(1-\hat{\rho}b_R N_A)^2} - \left[\frac{2\hat{\rho}a_R N_A^2 + \hat{\rho}^2 a_R b_R N_A^3}{T^{1/2}(1+\hat{\rho}b_R N_A)^2}\right] + \frac{\tilde{A}_{ll} N_A^2 \hat{\rho}}{3\pi z^3 \rho_{N,fc}^2}\left[1 - \frac{2D_f^6}{15z^6}\right] = 0 \quad (28)$$

Designating critical properties with a 'c' subscript, we now define reduced properties as

$$P_r = P/P_c, \quad T_r = T/T_c \quad (29)$$

$$\rho_r = \hat{\rho}/\hat{\rho}_c, \quad v_r = \hat{v}/\hat{v}_c \quad (30)$$

$$\mu_r = \hat{\mu}/RT_c \quad (31)$$

$$z_r = z/[k_B T_c/P_c]^{1/3} \quad (32)$$

Using the above relations to replace physical properties (P, T, etc.) with reduced ones (P_r, T_r, etc.), Eqs. (21), (22) and (28) can be converted to the dimensionless forms

$$P_r = \frac{3\rho_r T_r}{1-\rho_r b_r} - \frac{\rho_r^2 a_r}{T_r^{1/2}(1+\rho_r b_r)} + \frac{A'_{ll}\rho_r^2}{2\pi z_r^3}\left[1 - \frac{2D_{r,f}^6}{15z_r^6}\right] \quad (33)$$

$$\mu_r = -T_r\left[\frac{\xi-5}{2}\ln\pi - \ln\sigma_s\right] - T_r \ln\left[\frac{1-\rho_r b_r}{\rho_r N_A \hat{\rho}_c \Lambda^3}\right] + \frac{\rho_r b_r T_r}{1-\rho_r b_r} - \frac{(\xi-3)T_r}{2}\ln\left(\frac{T_r}{T_{r,\theta}}\right) - \frac{a_r}{3b_r T_r^{1/2}}\ln(1+\rho_r b_r) - \frac{a_r}{3T_r^{1/2}}\left(\frac{\rho_r}{1+\rho_r b_r}\right) + \frac{A'_{ll}\rho_r}{3\pi z_r^3}\left[1 - \frac{2D_{r,f}^6}{15z_r^6}\right] - \frac{A'_{ls}}{6\pi z_r^3}\left[1 - \frac{2D_{r,m}^6}{15z_r^6}\right] \quad (34)$$

$$\frac{3T_r}{(1-\rho_r b_r)^2} - \frac{a_r\rho_r(2+\rho_r b_r)}{T_r^{1/2}(1+\rho_r b_r)^2} + \frac{A'_{ll}\rho_r}{\pi z_r^3}\left[1 - \frac{2D_{r,f}^6}{15z_r^6}\right] = 0 \quad (35)$$

where

$$a_r = a_R N_A^2/(P_c T_c^{1/2}\hat{v}_c^2), \quad b_r = b_R N_A/\hat{v}_c \quad (36)$$

$$A'_{ll} = \tilde{A}_{ll}/k_B T_c, \quad A'_{ls} = \tilde{A}_{ls}/k_B T_c \quad (37)$$

$$D_{r,f} = D_f/[k_B T_c/P_c]^{1/3}, \quad D_{r,m} = D_m/[k_B T_c/P_c]^{1/3} \quad (38)$$

$$T_{r,\theta} = \theta_{rot,m}/T_c \quad (39)$$

Note that Eqs. (25), (26) and (36) imply that a_r and b_r are just the numerical constants specified below:

$$a_r = 3.84732, \quad b_r = 0.25992 \quad (40)$$

Use of the above three Eqs. (33)–(35) to predict near-wall effects on properties and the spinodal condition is discussed in the next section.

3. Model analysis of properties in the near-wall region

For fluid near the wall, thermodynamic equilibrium requires that the temperature and the chemical potential at each z location must equal their respective values in the bulk fluid. The pressure varies with distance from the solid wall due to the long-range attractive force exerted by the wall molecules on the fluid molecules. Note that this is qualitatively similar to the pressure gradient in a container of liquid in a gravitational field, although in that case the gravitational body force acting uniformly on all molecules produces a linear pressure profile in the fluid.

To determine the variation of properties in the near-wall region, the equilibrium requirements were invoked by following the following calculation sequence:

1. To model saturated liquid near a solid surface, the bulk fluid reduced pressure $P_{r,\infty}$ was specified and the bulk fluid reduced temperature was taken to be the corresponding reduced saturation temperature $T_{r,\infty} = T_{r,sat}(P_{r,\infty})$. $T_{r,\infty} = T_{r,sat}(P_{r,\infty})$ was determined as the value of reduced temperature that satisfies the equation of state at the specified $P_{r,\infty}$ and results in equality of reduced chemical potential for the liquid and vapor phases. The value of $T_{r,sat}(P_{r,\infty})$ that satisfies these requirements was determined using the iterative method proposed by Carey [9] with A'_{ll} and A'_{ls} set to zero in all equations. For subcooled liquid, the bulk fluid reduced pressure and temperature $P_{r,\infty}$ and $T_{r,\infty}$ were both specified. For the known $P_{r,\infty}$ and $T_{r,\infty}$ values, Eq. (33) was solved, with $A'_{ll} = 0$, to determine the bulk fluid density.
2. Using Eq. (34) to evaluate the chemical potential in the bulk fluid (at $\rho_{r,\infty}$ and $T_{r,\infty}$) and at the location of interest z_r, and requiring equality of chemical potential and temperature at the two locations, the following equation is obtained:

$$-T_{r,\infty}\ln\left[\frac{1-\rho_r b_r}{\rho_r N_A \hat{\rho}_c \Lambda^3}\right] + \frac{\rho_r b_r T_{r,\infty}}{1-\rho_r b_r} - \frac{a_r}{3b_r T_{r,\infty}^{1/2}}\ln(1+\rho_r b_r) - \frac{a_r}{3T_{r,\infty}^{1/2}}\left(\frac{\rho_r}{1+\rho_r b_r}\right) + \frac{A'_{ll}\rho_r}{3\pi z_r^3}\left[1 - \frac{2D_{r,f}^6}{15z_r^6}\right] - \frac{A'_{ls}}{6\pi z_r^3}\left[1 - \frac{2D_{r,fs}^6}{15z_r^6}\right] = -T_{r,\infty}\ln\left[\frac{1-\rho_{r,\infty} b_r}{\rho_{r,\infty} N_A \hat{\rho}_c \Lambda^3}\right] + \frac{\rho_{r,\infty} b_r T_{r,\infty}}{1-\rho_{r,\infty} b_r} - \frac{a_r}{3b_r T_{r,\infty}^{1/2}}\ln(1+\rho_{r,\infty} b_r) - \frac{a_r}{3T_{r,\infty}^{1/2}}\left(\frac{\rho_{r,\infty}}{1+\rho_{r,\infty} b_r}\right) \quad (41)$$

This equation was iteratively solved for the reduced density at location z_r.
3. With the local reduced temperature set to the bulk value and using the local reduced density determined in step 2, Eq. (33) was used to determine the local reduced pressure P_r.

Table 1
Fluid and wall parameters for typical systems

Fluid/surface combination	P_∞ (kPa)	$T_{sat}(P_\infty)$ (K)	σ_{lv} (N/m)	A_{ll} (10^{-20} J)	A_{ss} (10^{-20} J)	A_{sl} (10^{-20} J)	D_f (nm)	D_m (nm)
Saturated CCl_4 liquid near a gold surface	101.3	350.0	0.0202	4.147	40	12.88	0.56	0.45
Saturated liquid water near a gold surface	101.3	373.2	0.0589	12.09	40	21.99	0.28	0.31
Saturated O_2 liquid near a gold surface	101.3	90.2	0.0132	2.708	40	10.41	0.36	0.35
Saturated Ar liquid near a gold surface	101.3	87.3	0.0125	2.572	40	10.14	0.38	0.34

4. The spinodal limit at the specified location was determined by simultaneous solution of Eqs. (33) and (35) for the spinodal reduced density and temperature, $\rho_{r,spin}$ and $T_{r,spin}$, at the local reduced pressure P_r determined in step 3. These equations were solved using a Newton–Raphson iterative scheme. Convergence of the scheme was achieved when the absolute value of the left side of Eq. (35) was less than 10^{-12}.

In this investigation, we were particularly interested in systems that exhibit strong near-wall effects. Table 1 shows estimated values of fluid and wall parameters for four example systems. These four were considered because they include examples of three categories of systems. The metallic gold surface was considered because atoms in metals generally exert high long-range attraction forces on common fluid molecules. The Hamaker constant for two identical pure metallic solid surfaces (gold, silver, copper) is estimated to be between 30×10^{-20} and 50×10^{-20} J [6]. The value of A_{ss} was taken to be 40×10^{-20} J in this study. The parameters D_m and D_f were estimated using values of effective atomic and molecular radii recommended in the literature [6].

As discussed by Israelachvilli [6], several methods of predicting Hamaker constants have been proposed. The values for liquid–liquid and liquid–solid Hamaker constants, A_{ll} and A_{ls}, in Table 1 were computed using the relations summarized by Israelachvilli [6]:

$$A_{ll} = 24\pi D_0^2\sigma_{lv}, \quad A_{ls} = \sqrt{A_{ll}A_{ss}} \tag{42}$$

In the above equations, σ_{lv} is the interfacial tension at the system temperature, and D_0 is the cutoff separation of 0.165 nm.

Table 2
Fluid critical parameters

Fluid	T_c (K)	P_c (MPa)	$(k_BT_c/P_c)^{1/3}$ (nm)
CCl_4	556.4	4.560	1.190
Water	647.3	22.129	0.739
O_2	154.8	5.090	0.749
Ar	150.7	4.860	0.753

The critical properties in Table 2 were used to convert the physical parameters in Table 1 to the corresponding dimensionless parameters in Table 3. Using the computational scheme described above, the variations of density, pressure and spinodal temperature with distance from the solid wall in the liquid were determined for the four example systems listed in Table 3. The resulting variations of pressure and spinodal temperature for three of these systems are plotted in Figs. 3–5. As can be seen, the pressure and spinodal temperature differ from the bulk values only in the region very close to the solid surface. The density similarly differs significantly from the bulk value only in the region very close to the solid surface. In all three systems the characteristic length $[k_BT_c/P_c]^{1/3}$ is close to one nanometer (see Table 2). The variations plotted in Figs. 3–5 indicate that the wall interaction significantly affects the properties only within a few nanometers of the wall.

4. Verification of the pressure profile in the near-wall region

The variation of pressure near the wall that is predicted by our model differs substantially from that

Table 3
Dimensionless wall effect parameters for typical systems

Fluid/surface combination	P_∞ (kPa)	$P_{r,\infty}$	$T_{r,sat}$ ($P_{r,\infty}$)	A'_{ll}	A'_{sl}	$D_{r,f}$	$D_{r,m}$
Saturated CCl_4 liquid near a gold surface	101.3	0.02222	0.6047	0.5948	5.568	0.471	0.374
Saturated liquid water near a gold surface	101.3	0.004578	0.5273	1.331	7.720	0.379	0.413
Saturated O_2 liquid near a gold surface	101.3	0.01990	0.5984	1.382	16.09	0.481	0.461
Saturated Ar liquid near a gold surface	101.3	0.02078	0.6009	1.354	16.14	0.505	0.471

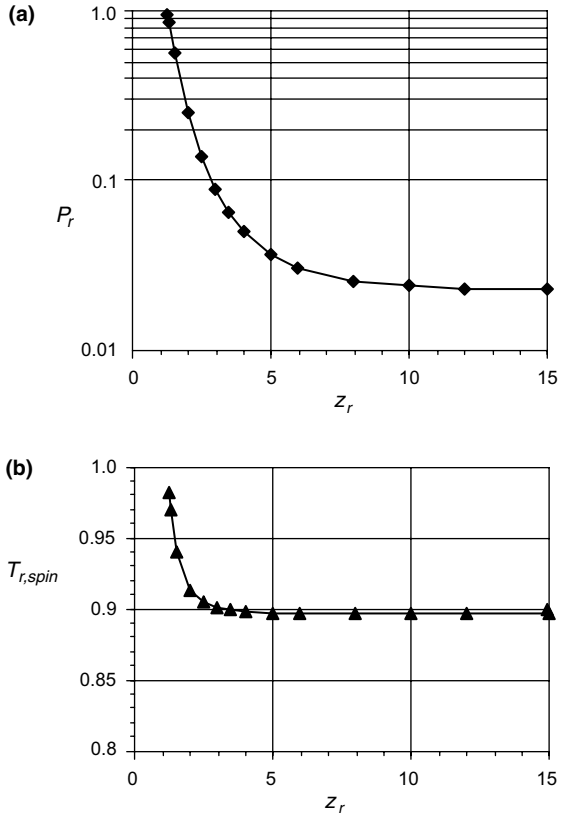

Fig. 3. Saturated liquid CCl_4 at 101 kPa on gold.

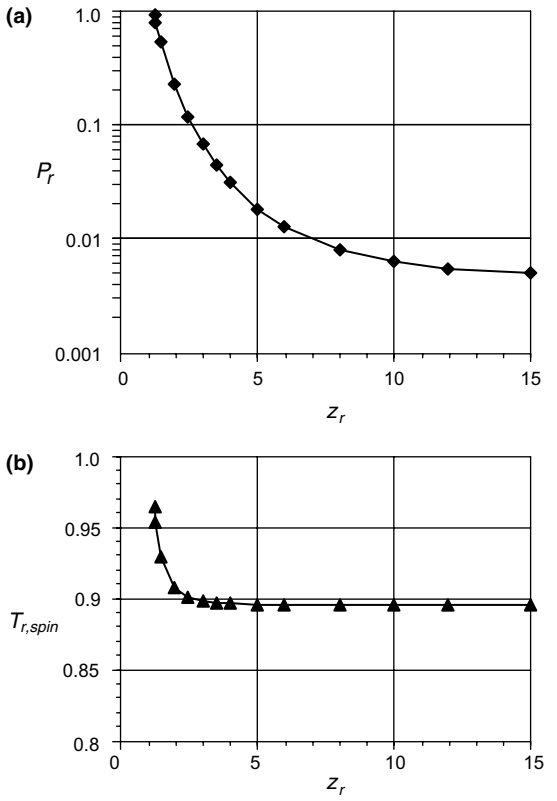

Fig. 4. Saturated liquid water at 101 kPa on gold.

predicted by the model of Gerweck and Yadigaroglu [7]. We have therefore examined this issue using two other methods of analysis. The first alternate approach is to predict the pressure variation using a continuum (mean field) hydrostatic model. This amounts to using an applied wall potential to determine the body force in the Navier–Stokes equations with no velocity terms,

$$0 = -\frac{1}{\rho_{\mathrm{m,f}}}\nabla P + \vec{f}_{\mathrm{fs}} \tag{43}$$

In the above equation, $\rho_{\mathrm{m,f}}$ is the fluid mass density and $\vec{f}_{\mathrm{fs}}$ is the force per unit mass on the fluid system. Eq. (5) provides the potential function that dictates the force interaction between a solid molecule and a fluid molecule. It follows from Eq. (8) that the mean-field potential energy felt by the fluid molecule due to interactions with all the solid molecules is

$$\begin{aligned}\Phi_{\mathrm{fmf}} &= 2\pi\rho_{N,\mathrm{s}}\int_{z_{\mathrm{s}}=z}^{\infty}\int_{x=0}^{\infty}\phi_{\mathrm{fs}}x\,\mathrm{d}x\,\mathrm{d}z_{\mathrm{s}} \\ &= -\frac{\pi\rho_{N,\mathrm{s}}C_{\phi,\mathrm{fs}}}{6z^3}+\frac{\pi\rho_{N,\mathrm{s}}C_{\phi,\mathrm{fs}}D_{\mathrm{m}}^6}{45z^9}\end{aligned} \tag{44}$$

Combining Eqs. (13) and (44) yields

$$\Phi_{\mathrm{fmf}} = \frac{A_{\mathrm{ls}}}{6\pi\rho_{N,\mathrm{f}}D_{\mathrm{m}}^3}\left[\frac{2}{15}\left(\frac{D_{\mathrm{m}}}{z}\right)^9-\left(\frac{D_{\mathrm{m}}}{z}\right)^3\right] \tag{45}$$

It follows that the force felt by a single molecule due to the entire wall is given by $\vec{F}_{\mathrm{fs}} = -\nabla\Phi_{\mathrm{fmf}}$, and the corresponding force per unit mass is

$$\vec{f}_{\mathrm{fs}} = \frac{\vec{F}_{\mathrm{fs}}}{M} = \frac{A_{\mathrm{ls}}}{2\pi\rho_{\mathrm{m,f}}D_{\mathrm{m}}^4}\left[\frac{2}{5}\left(\frac{D_{\mathrm{m}}}{z}\right)^{10}-\left(\frac{D_{\mathrm{m}}}{z}\right)^4\right]\vec{z} \tag{46}$$

where $\vec{z}$ is the unit vector in the z-direction. The force per unit mass specified by Eq. (46) is substituted into Eq. (43), and since the force only acts in the z-direction, the relation simplifies to

$$\frac{\mathrm{d}P}{\mathrm{d}z} = \frac{A_{\mathrm{ls}}}{2\pi D_{\mathrm{m}}^4}\left[\frac{2}{5}\left(\frac{D_{\mathrm{m}}}{z}\right)^{10}-\left(\frac{D_{\mathrm{m}}}{z}\right)^4\right] \tag{47}$$

Integrating both sides of Eq. (47) from a position z to ∞, and taking the pressure at ∞ to be P_∞, the resultant expression for the pressure profile is

$$P(z) = P_\infty - \frac{A_{\mathrm{ls}}}{6\pi D_{\mathrm{m}}^3}\left[\frac{2}{15}\left(\frac{D_{\mathrm{m}}}{z}\right)^9-\left(\frac{D_{\mathrm{m}}}{z}\right)^3\right] \tag{48}$$

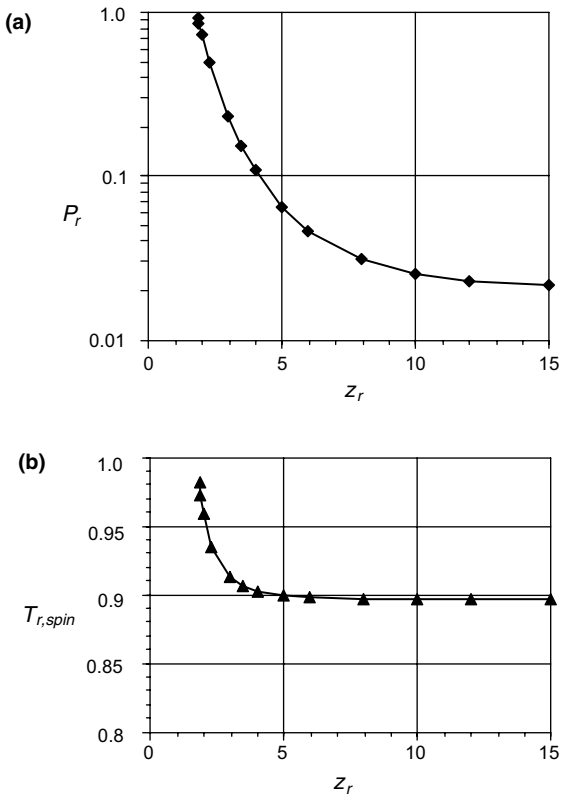

Fig. 5. Saturated liquid oxygen at 101 kPa on gold.

As a second means of assessing the validity of the pressure profile predicted by our thermodynamic model, we also modeled the molecular level behavior of liquid argon near a solid gold (metallic) wall using a classical molecular dynamics (MD) simulation. A hybrid molecular dynamics simulation was used that combined a traditional NVE-type MD simulation technique with stochastic boundary conditions used to simulate a solid wall at $z \leqslant 0$ and a surrounding saturated vapor with a pressure of 1 atm for $z > L$ (see Fig. 6). Argon molecules in the system move according to Newton's laws of motion, and these molecules interacted via the well-known Lennard-Jones 6–12 potential,

$$\phi_{\mathrm{LJ},ij}(r_{ij}) = 4\varepsilon_{\mathrm{LJ}}\left[\left(\frac{\sigma_{\mathrm{LJ}}}{r_{ij}}\right)^{12} - \left(\frac{\sigma_{\mathrm{LJ}}}{r_{ij}}\right)^{6}\right] \tag{49}$$

where σ_{LJ} and $\varepsilon_{\mathrm{LJ}}$ are the Lennard-Jones length and energy parameters, respectively, and r_{ij} is the distance between molecules i and j. In this study, σ_{LJ} and $\varepsilon_{\mathrm{LJ}}$ were taken to be 0.3405 nm and 1.64×10^{-21} J, respectively, for argon. Both the forces and intermolecular potentials were smoothly truncated at the cutoff radius of $4.2\sigma_{\mathrm{LJ}}$. The time step used in the simulations was 5 fs, and the configuration was updated at each step by the velocity Verlet algorithm [10].

The hybrid MD simulation domain utilized in this study, depicted in Fig. 6, featured three types of boundaries: periodic, wall, and (molecular) flux. Periodic boundaries existed at all four boundaries in the x and y directions. The $z = 0$ boundary represented the solid surface and featured a wall potential which bound the liquid film to a semi-infinite metal solid. The external force on each molecule in this simulation was computed as the negative gradient of the wall potential $\vec{F}_{\mathrm{fs}} = -\nabla\Phi_{\mathrm{fmf}}$ using Eq. (45).

The flux boundary treatment stochastically injects molecules as if the boundary were in contact with an infinite external bath of vapor held at atmospheric pressure. The system was initialized with 2000 molecules, but the flux boundary treatment allowed for variation in the system molecule count as the simulation progressed. The thickness of the liquid film was initialized to be approximately 12 nm, which is large enough to appropriately simulate a bulk liquid since the wall-affected and interfacial regions occupy approximately 1 nm and 2 nm of the thickness, respectively. The system temperature was ramped up to the desired value using velocity rescaling for the initial 50,000 time steps, and the system was then allowed to stabilize to an equilibrium state for an additional 50,000 time steps before collecting property data. Further details on this type of this simulation methodology are described by Wemhoff and Carey [11].

Upon equilibration, the simulation domain was evenly divided into 50 cells along the z-axis for collection of pressure values for the final 200,000 steps of the simulation. The local pressure in the z-direction was determined using the modified virial calculation proposed

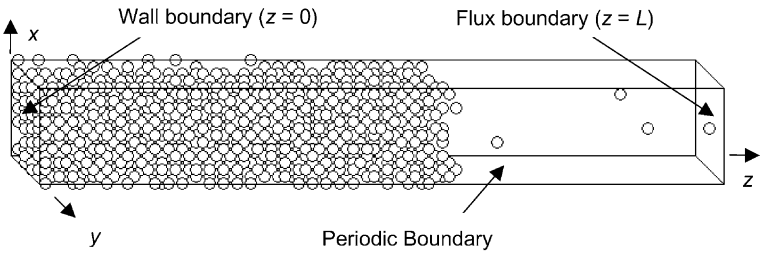

Fig. 6. MD simulation domain and boundary conditions.

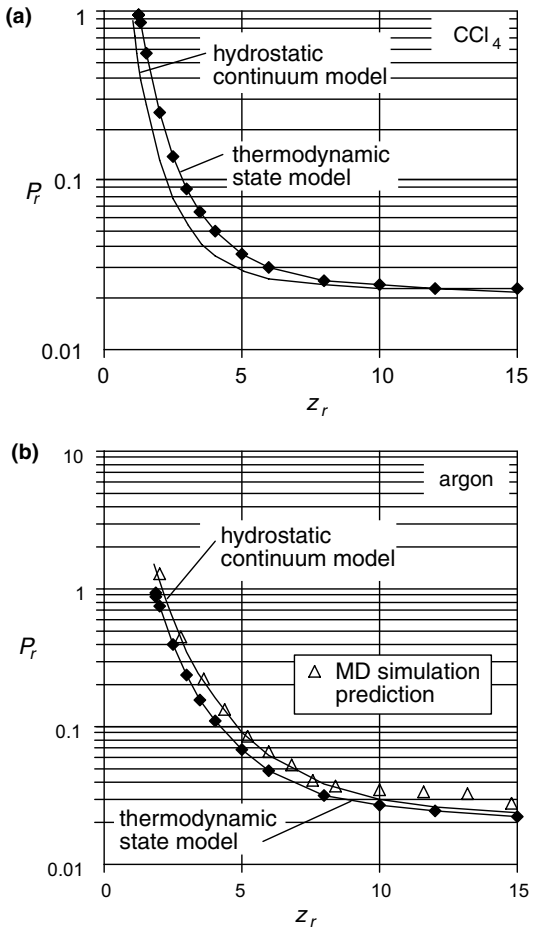

Fig. 7. Pressure profiles for (a) liquid CCl_4 and (b) liquid argon at 101 kPa on gold.

by Weng et al. [12]. The local pressure was assumed to be isotropic since the simulation had attained local thermodynamic equilibrium.

Fig. 7a shows the pressure profile predicted by the hydrostatic relation (48) for carbon tetrachloride using the values of A_{ls} and D_m from Table 1, with P_∞ set to 1 atm. Also shown in this figure is the pressure profile predicted by the thermodynamic model for the same conditions. It can be seen that the pressure profile predicted by the hydrostatic continuum model agrees well with that predicted by the thermodynamic property model. This level of agreement was also found for comparisons of the predicted pressure profiles for oxygen and water at the conditions in Table 1.

Fig. 7b shows the pressure profile in the wall-affected region predicted by the MD study for argon. Also shown are the pressure variations predicted using the continuum hydrostatic model and the thermodynamic property analysis developed here for the parameter values listed in Tables 1 and 3 for argon near a gold surface. The figure indicates that the predicted pressure profiles for all these models agree fairly well, suggesting that our thermodynamic model of properties near the wall provides a physically correct prediction of the pressure variation in the near-wall region.

The increase in pressure near the wall is similar to the effect of gravity on a fluid near the bottom of an upward-facing container, except that the effect is more localized because the attractive force decays rapidly with distance from the wall. The predicted increase in the spinodal temperature near the wall implies that the fluid there must be heated to a higher temperature to initiate homogeneous nucleation. The near-wall variation of the local spinodal temperature predicted by the model suggests that wall-interactions may affect the initiation of boiling during rapid pulse heating of a liquid near a solid heater surface. This is explored further in the next section.

5. Onset of homogeneous nucleation during rapid pulse heating

As noted in Section 1, a number of previous theoretical and experimental investigations have indicated that homogeneous nucleation plays at least a partial role in boiling onset during rapid transient heating of a liquid. Several more recent investigations of this type of process have focused on conditions similar to those at heater elements in thermal inkjet printing [2–4,13]. Here we will examine the role of wall effects on the type of sudden rapid heating encountered in ink jet printers.

In inkjet printing systems, nucleation is generally a consequence of heat generation from a thin film heater on a solid substrate in contact with an extensive liquid pool. The simplest model of this heating process is the sudden application of a constant heat flux at the $z = 0$ plane between a semi-infinite body of solid and a semi-infinite body of liquid (see Fig. 8). The well-known constant-property continuum model for this process is

$$\text{for } z < 0\text{:}\quad \frac{\partial T}{\partial t} = \alpha_s \frac{\partial^2 T}{\partial z^2} \tag{50a}$$

$$\text{at } t = 0\text{: } T = T_\infty \text{ (for } z < 0\text{)},$$

$$\text{as } z \to -\infty : T = T_\infty \tag{50b}$$

$$\text{for } z > 0\text{:}\quad \frac{\partial T}{\partial t} = \alpha_l \frac{\partial^2 T}{\partial z^2} \tag{51a}$$

$$\text{at } t = 0\text{: } T = T_\infty \text{ (for } z > 0\text{)},$$

$$\text{as } z \to \infty\text{: } T = T_\infty \tag{51b}$$

$$\text{at } z = 0\text{: } q''_w = -k_s \left(\frac{\partial T}{\partial z}\right)_{z=0-} - k_l \left(\frac{\partial T}{\partial z}\right)_{z=0+} \tag{52}$$

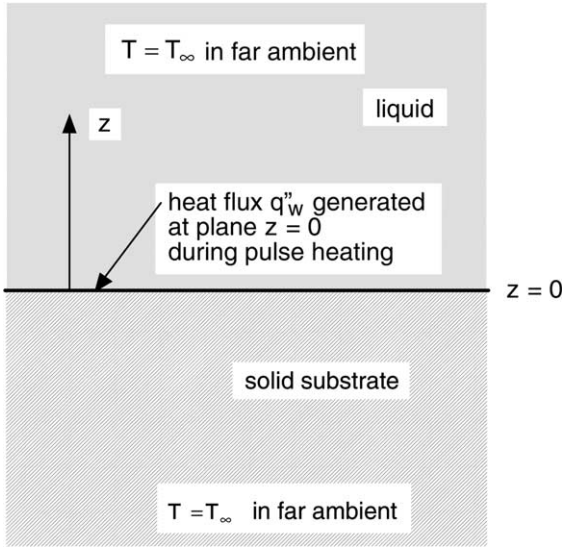

Fig. 8. Schematic for analysis of pulsed heating at the solid–liquid interface.

The solution for this system dictates that the portion of the applied heat flux that enters the liquid $q''_l = -k_l(\partial T/\partial z)_{z=0+}$ is given by

$$q''_l = \frac{q''_w}{1 + (k_s/k_l)\sqrt{(\alpha_l/\alpha_s)}} \tag{53}$$

The solution for the temperature field in the liquid can be expressed in the form

$$T = T_\infty + \frac{q''_l}{k}\int_z^\infty \mathrm{erfc}\left(\frac{\hat{z}}{2\sqrt{\alpha_l t}}\right)\mathrm{d}\hat{z} \tag{54}$$

Expanding this solution near $z = 0$, the following expression is obtained for the solution in the near-wall region:

$$T = T_\infty + \frac{2q''_l}{k_l}\sqrt{\frac{\alpha_l t}{\pi}} - \frac{q''_l z}{k_l} + \frac{z^3}{6\sqrt{\pi}\alpha_l t} + \cdots \tag{55}$$

The above expansion solution reflects the fact that the surface temperature increases proportional to $\sqrt{t}$, and the temperature profile is essentially linear at small z (large Fourier number $\alpha_l t/z^2$).

To examine the role of wall force interactions on the onset of nucleation during rapid transient heating, the thermodynamic model described above was used to predict the property variations in the near-wall region in the fluid before the transient heating was initiated. The property variations were computed for water at bulk conditions typical of an inkjet printer system: $P_\infty = 101$ kPa and $T_\infty = 313.2$ K. The water properties in Table 4 were used in this computation. The resulting reduced pressure and spinodal temperature variations near the surface are shown in Fig. 9. These results exhibit the same qualitative trends as the variations for saturated liquids shown in Figs. 3–5.

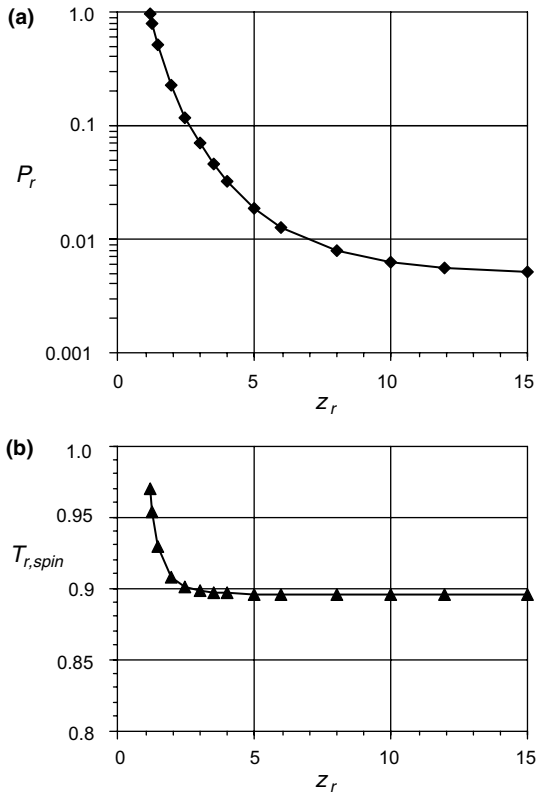

Fig. 9. Subcooled liquid water at 101 kPa and 40 °C on gold.

The results were computed for water at atmospheric pressure and 313.2 K (40 °C) to facilitate a comparison with the observations of Rembe et al. [13] for rapid transient heating of water at atmospheric pressure. In their investigation, Rembe et al. [13] used a pseudo-cinematographic visualization technique to observe the onset of nucleation near a thin film heater between a solid substrate and a reservoir of pure water. The heater was 60 μm square. The film heater was the type used in Hewlett-Packard deskjet printers. Their pseudo-cinematographic visualization technique required repeated

Table 4
Parameters for subcooled water system

Fluid/surface combination	P_∞ (kPa)	T_∞ (K)	$P_{r,\infty}$	$T_{r,\infty}$	A'_{ll}	A'_{sl}	$D_{r,f}$	$D_{r,m}$
Subcooled liquid water near a gold surface	101.3	313.2	0.004578	0.4839	1.331	7.720	0.379	0.413

application of power to the heater to collect images of the process at different times. The total power input of 7.5 W was applied for 3 μs. Because the repeated heating is expected to raise the temperature of the water in the reservoir above room temperature, a bulk water temperature of 40 °C was assumed for the comparison here. This is consistent with estimates of the ink temperature during printer operation [14].

During the 3 μs heating process in the experiments by Rembe et al. [13], the 7.5 W input corresponds to a total heat flux of 2.08×10^9 W/m^2 over the 60 μm × 60 μm heater. Using the properties of water and silicon at 400 K to represent the properties of the solid substrate under the heater and the adjacent water [15,16], the properties in Eq. (53) were estimated to be: $k_l = 0.674$ W/mK, $\alpha_l = 1.72 \times 10^{-7}$ m^2/s, $k_s = 89.7$ W/mK, and $\alpha_s = 4.76 \times 10^{-5}$ m^2/s. Using these properties in Eq. (53) and the total input flux of 2.08×10^9 W/m^2, the heat flux into the liquid is $q''_l = 2.31 \times 10^8$ W/m^2. This value of q''_l and the properties for the liquid and solid can be substituted into Eq. (55) to predict the variation of the near-wall temperature profile with time during the heating transient. Some of the resulting profiles are shown in Fig. 10. Also shown in Fig. 10 are observations of the onset of nucleation at 2.5 μs and the explosive vaporization and vapor blanketing observed at 3 μs. As expected, the temperature profile, which is nominally linear in z, shifts upward with time,

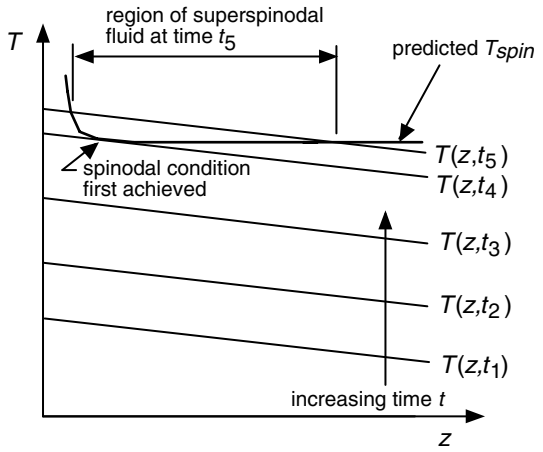

Fig. 11. Schematic of near-wall temperature variation and the approach to the spinodal condition.

as indicated schematically in Fig. 11. Note that because the temperature profile has a slightly negative slope and the local spinodal temperature increases as z decreases, the spinodal condition will first be achieved when the temperature profile first crosses the spinodal curve at a location a few nanometers away from the surface. This is indicated schematically in Fig. 11. This suggests that homogeneous nucleation is most likely to be

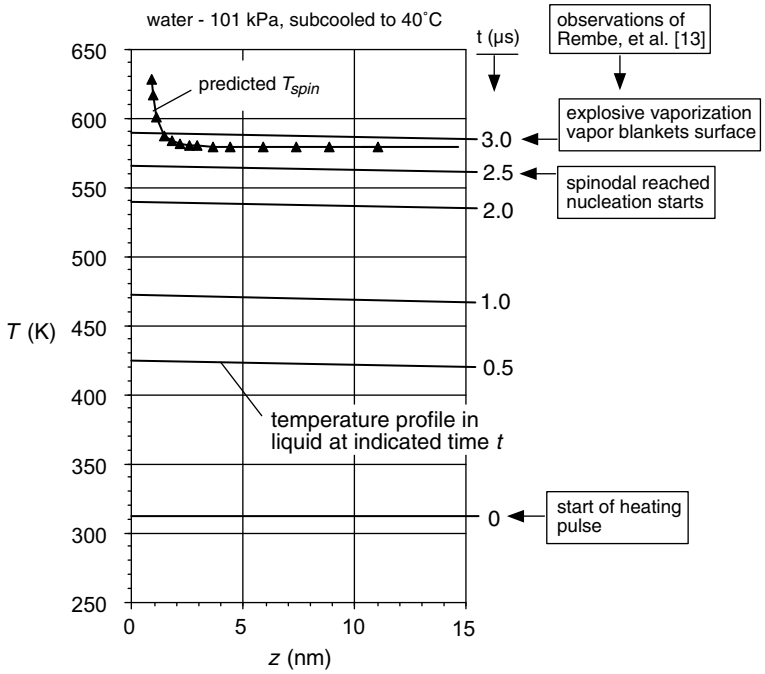

Fig. 10. Liquid temperature profile variation due to pulsed heating and associated experimental observations for the conditions in the experiments of Rembe et al. [13].

observed first at this location. If nucleation does not occur immediately when the temperature profile first intersects the spinodal curve, the temperature profile could continue to increase, as shown in Fig. 11, creating a region of superspinodal fluid.

Generally, the spinodal condition is interpreted as a limit at which a phase change must occur. However, this may not be so for the rapid transient heating process considered here. Actually, models of the kinetic limit of superheat predict that the rate of critical embryo generation increases rapidly with temperature. The theory formulated by Katz and Blander [17] predicts that the rate of formation of embryos of critical size J (number/m^3 s) is given by

$$J = \frac{N_A}{\hat{v}_l}\left(\frac{3\sigma_{lv}}{\pi M}\right)^{1/2} \times \exp\left\{\frac{-16\pi\sigma_{lv}^3}{3k_B T[P_{sat}(T)\exp\{\hat{v}_l[P-P_{sat}(T)]/RT\}-P]^2}\right\} \quad (56)$$

where $\hat{v}_l$ is molar specific volume of the liquid. The onset of nucleation is usually taken to correspond to conditions that result in an embryo formation rate of $J = 10^{12}$ m^{-3} s. When a liquid is slowly heated, the onset of nucleation may be observed at a lower temperature, where the embryo generation rate is lower, because more time is available for observation of a nucleation event. During rapid heating in the small systems of interest here, the embryo generation rate corresponding to the spinodal condition may not produce an observable nucleation event before the temperature profile increases significantly above the spinodal. The resulting profile would be like that at $t = t_5$ in Fig. 11. The range of z for which the local temperature is above T_{spin} defines a layer of superspinodal fluid. As the temperature increases beyond T_{spin}, kinetic limit theory (Eq. (56)) predicts that the rate of embryo production rises rapidly, which would eventually produce an embryo that would trigger the onset of nucleation [18].

The observations of Rembe et al. [13] are consistent with the scenario described above. As indicated in Fig. 10, they observed the first nucleation at 2.5 μs into the heating process. The model analysis developed here predicts that the local temperature will equal the spinodal temperature at about 2.8 μs, which is very close to the observed time of onset of nucleation. Full blanketing of the surface by vapor was observed to occur at 3.0 μs into the heating process. The model indicates that during the time between onset ($t = 2.5$ μs) and blanketing ($t = 3.0$ μs), some regions of the fluid may have heated slightly above the spinodal temperature. The large increase in the embryo generation rate associated with this additional superheating may be a primary mechanism in the rapid and extensive vapor generation, surface blanketing and explosive vaporization that were subsequently observed.

6. Concluding remarks

Although it is based on the simple Redlich–Kwong fluid model, the model developed here provides a means of predicting near-wall effects on fluid properties for a wide variety of fluids. This model has the advantage that it can be cast in terms of reduced properties and the wall effects are quantified in terms of modified Hamaker constants, making it possible to easily apply the model to a wide variety of fluid and solid combinations.

The model analysis of wall interaction effects on properties has been applied to a metallic solid wall in contact with several different fluids, including a polar molecule (water), non-polar molecule (CCl_4) and a cryogenic fluid with a low critical temperature. Two interesting predictions of the model are that as the wall is approached ($z \to 0$) the local pressure and the local spinodal temperature increase rapidly in the region within a few nanometers of the wall. The rise in pressure is consistent with the predictions of the model of near-wall effects developed by Gerweck and Yadigaroglu [7]. The model of Gerweck and Yadigaroglu [7] also predicts a region of negative pressure further from the surface that this model does not. This difference appears to be a result of the different wall-molecule interaction potentials used in the two models. The increase in pressure near the wall is similar to the rise in pressure caused by gravity forces acting on fluid molecules above a horizontal solid surface. The only difference here is that the attractive forces are negligible beyond a few nanometers from the wall, so the rise in pressure is limited to that region.

The near-wall pressure variations determined by a continuum hydrostatic model and an MD simulation agreed well with the pressure variation predicted by our thermodynamic property model. This supports the contention that our thermodynamic model predictions of a monotonically increasing pressure profile near the wall are at least qualitatively correct for real fluids of the types considered here.

The near-wall property model developed here predicts that during rapid transient pulse heating, the spinodal condition will be first achieved at a location a few nanometers away from the surface. For such processes in inkjet printers, this appears to enhance the tendency for initiation of homogeneous nucleation in a liquid layer a few nanometers away from the solid heater and the subsequent vapor blanketing and explosive vaporization over the surface. Our theoretical analysis of the rapid transient heating of water, including the predicted variation of the spinodal temperature due to wall effects, is consistent with the observed onset and explosive vaporization in the experiments of Rembe et al. [13].

Overall, the near-wall property model indicates that, in most systems of interest, near-wall effects on nucleation and boiling are confined to the region within a few nanometers of the surface. In many systems, the surface roughness has a scale much larger than this (on the scale of microns, typically), implying the wall interaction effects would be difficult to separate from roughness effects. It further suggests, however, that wall interactions may play a distinct role in micro- and nanoscale systems in which surface geometries may be defined to smaller resolutions. Even a surface manufactured with nanoscale precision could have a roughness level that is comparable to or larger than the thickness of the wall-affected region. In such a circumstance, the wall-affected region presumably would follow the contours of the surface, as depicted in Fig. 12. Our model analysis implies that the spinodal temperature T_{spin} in the bulk liquid is lower than in the wall-affected region, and in deep cavities in the surface, like location A in Fig. 12, a protrusion of low T_{spin} bulk fluid may extend down into the cavity. Sudden initiation of heat generation in the solid will initiate transient conduction of heat into the adjacent liquid. Because the protrusion of low T_{spin} fluid in the cavity is nearly surrounded by solid surface, the tip of this protrusion may be heated to a temperature above T_{spin} before the temperature of fluid at other locations reaches the spinodal temperature. This suggests that a small cavity containing a protrusion of low T_{spin} fluid would be a preferred homogeneous nucleation site in rapid transient heating.

In their rapid heating experiments, O'Horo and Andrews [4] reported observing repeated early nucleation at specific locations on the surface. Repeated nucleation at a fixed location is often attributed to heterogeneous nucleation. The results of our analysis suggest that there is another possibility. The observed repeated early nucleation at fixed locations may be a consequence of homogeneous nucleation at preferred sites where high T_{spin} fluid penetrates into a deep cavity.

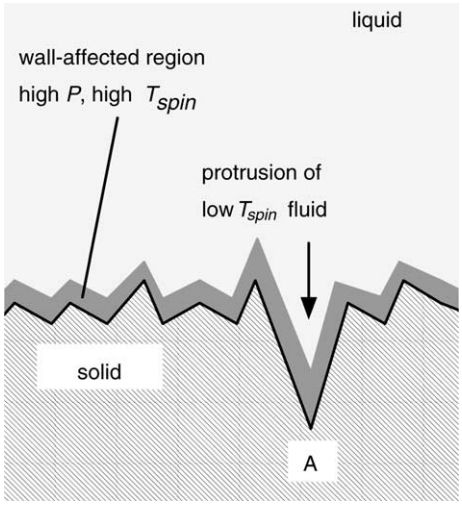

Fig. 12. Schematic of the wall affected region near a rough surface.

Acknowledgements

The authors acknowledge support for this research under the University of California MICRO Program. Access to the Millennium workstation cluster at UC Berkeley for the MD simulation studies is also appreciated.

References

[1] V.P. Skripov, Metastable Liquids, John Wiley & Sons, New York, 1974 (Chapters 3, 6).
[2] A. Asai, Bubble dynamics in boiling under high heat flux pulse heating, ASME J. Heat Transfer 113 (1991) 973–979.
[3] J.R. Andrews, M.P. O'Horo, High speed stroboscopic system for visualization of thermal inkjet processes, in: J. Bares (Ed.), Proceedings, Society of Photo-Optical Instrumentation Engineers (SPIE), vol. 2413, 1995, pp. 176–181.
[4] M.P. O'Horo, J.R. Andrews, Initial stages of vapor bubble nucleation in thermal ink jet processes, in: J. Bares (Ed.), Proceedings, Society of Photo-Optical Instrumentation Engineers (SPIE), vol. 2413, 1995, pp. 182–188.
[5] L. Lin, A.P. Pisano, V.P. Carey, Thermal bubble formation on polysilicon microresistors, ASME J. Heat Transfer 120 (1998) 735–742.
[6] J. Israelachvilli, Intermolecular & Surface Forces, second ed., Academic Press, 1994 (Chapter 11).
[7] V. Gerweck, G. Yadigaroglu, A local equation of state for fluid in the presence of a wall and its application to rewetting, Int. J. Heat Mass Transfer 35 (1992) 1823–1832.
[8] V.P. Carey, Statistical Thermodynamics and Microscale Thermophysics, Cambridge University Press, 1999 (Chapter 6).
[9] V.P. Carey, Thermodynamic properties and structure of the liquid–vapor interface: a neoclassical Redlich–Kwong model, J. Chem. Phys. 118 (2003) 5053–5064.
[10] M.P. Allen, D.J. Tildesley, Computer Simulation of Liquids, Clarendon Press, Oxford, UK, 1987 (Chapter 3).
[11] A.P. Wemhoff, V.P. Carey, Exploration of nanoscale features of thin liquid films on solid surfaces using molecular dynamics simulations, in: Proceedings of 2004 International Mechanical Engineering Congress and Exposition, ASME, New York, 2004, , paper IMECE2004-59429.
[12] J.G. Weng, S. Park, J.R. Lukes, C.L. Tien, Molecular dynamics investigation of thickness effect on liquid films, J. Chem. Phys. 113 (2000) 5917–5923.
[13] C. Rembe, S. aus der Wiesche, E.P. Hofer, Thermal ink jet dynamics: modeling, simulation and testing, Microelectron. Reliab. 40 (2000) 525–532.
[14] hp.com, Myths about thermal inkjet printing, accessed online October 14, 2004. Available from: <http://www.hp.com/oeminkjet/learn/myths.html>.

[15] Y.S. Touloukian, C.Y. Ho (Eds.), Thermophysical Properties of Matter, vols. 1 & 4, Plenum Press, New York, 1972.
[16] F.P. Incropera, D.P. DeWitt, Fundamentals of Heat and Mass Transfer, fifth ed., John Wiley & Sons, New York, 2002 (Appendix A).
[17] J.L. Katz, M. Blander, Condensation and boiling: corrections to homogeneous nucleation theory for nonideal gases, J. Colloid Interface Sci. 42 (1973) 496–502.
[18] V.P. Carey, Liquid–Vapor Phase-Change Phenomena, Taylor and Francis, New York, 1992 (Chapter 5).